IEEE Access
Multidisciplinary | Rapid Review | Open Access Journal

Received October 5, 2020, accepted October 18, 2020, date of publication October 26, 2020, date of current version November 6, 2020.

Digital Object Identifier 10.1109/ACCESS.2020.3034018

A Fast Inverse Scattering Imaging Method by Applying Virtual Experiments to T-Matrix Scheme

YONGJI GAN[1], CHENGYOU YIN[1], QIMENG FAN[2], AND ANQI LI[1]
[1]College of Electronics Engineering, National University of Defense Technology, Hefei 230031, China
[2]High-Tech Institute of Xi'an, Xi'an 710025, China

Corresponding author: Chengyou Yin (cyouyin@sina.com)

ABSTRACT As a non-iterative linear inverse scattering imaging method, the linear sampling method (LSM) has the merits of easy implementation and high computational efficiency. In this article, based on the LSM and T-matrix method, we propose a fast method to reconstruct the target medium parameters. First, we use the LSM qualitative imaging method to estimate the contour of the target. Then, the preprocessing information of the LSM is applied to the virtual experiment circles in the framework of T-matrix method. In this way, we avoid the inversion of the matrix and only need to solve a series of univariate equations. Numerical simulation results show that the reconstruction accuracy of the proposed method is similar to that of LSM quantitative imaging method, but it has higher calculation accuracy and wider application range. Although the calculation accuracy is not as good as the contrast source inversion (CSI) method, the proposed method has huge advantages in terms of calculation efficiency.

INDEX TERMS Electromagnetic inverse scattering, linear sampling method, microwave imaging, T-matrix, virtual experiments.

I. INTRODUCTION

Electromagnetic inverse scattering is dedicated to reconstructing the characteristics of the object from the measured scattered field data. It has a wide range of applications in biomedical imaging, ground-penetrating radar, non-destructive testing, through-the-wall imaging, and so forth [1]–[4]. As a typical inverse problem, electromagnetic inverse scattering has two major characteristics: nonlinearity and ill-posedness [5].

According to the way of dealing with nonlinearity, traditional inverse scattering imaging methods can be divided into linear methods and nonlinear methods. Linear methods include Born approximation (BA) [6], Rytov approximation [7], and iterative methods derived from these two methods [8], [9]. They generally linearize the problem through field approximation. Although these methods are simple and easy to implement, they are only suitable for weak scatterers, that is, objects with small size and contrast. Literature [10] indicates that BA is only suitable for objects whose size and refractive index product does not exceed $0.35\lambda_b$. Nonlinear methods include modified gradient method (MGM) [11], contrast source inversion (CSI) method [12], [13], subspace optimization method (SOM) [14], and so on. Unlike linear methods, these methods use iteration to optimize reconstruction results. Since there is no approximation, nonlinear methods usually have higher reconstruction accuracy. The disadvantage of nonlinear methods is that they have a heavy computational burden. In addition, the nonlinearity methods depend on the initial value of the iteration, a bad initial selection may cause the iterative process to fall into a local optimum [15].

In addition to the quantitative inversion methods mentioned above, there is a class of methods called qualitative inversion methods, such as linear sampling method (LSM) [16]–[19] and factorization method [20]. The so-called qualitative approaches mean only retrieving information such as the target's position and profile, but not directly retrieving the target's electromagnetic parameters. LSM can obtain the target's morphology

The associate editor coordinating the review of this manuscript and approving it for publication was Mohamed Kheir.

by solving the indicator function related to the target position. Since there is no approximation, LSM is widely used in various targets including metal objects.

In recent years, on the basis of LSM qualitative inversion method, LSM has also begun to be used in quantitative imaging through virtual experiments and postprocessing strategies. The virtual experiment is a process of weighted combination of the original measurements, so that the rearranged scattered field or contrast source meets specific characteristics, and these specific field or contrast sources are beneficial to the inversion of target. By specifying different characteristics of the rearranged scattered field or contrast source, different virtual experiment strategies have been produced [21]–[23]. It is worth noting that the virtual experiment itself will not bring additional target information, but in this process, the morphology information of the target obtained by LSM is used as a priori information.

In literature [21], by applying virtual experiment and introducing a convenient total field approximation, the measurement equation is transformed into a linear equation. The linearization is achieved by replacing the unknown total field with the LSM preprocessing result, which has considered the scattering effect in the imaging domain. However, literature [24] pointed out that the total field approximation in [21] is only applicable for targets whose size and refractive index product is less than $1.22\lambda_b$. In this article, we apply the total field approximation to the framework of T-matrix method [25], but not based on the measurement equation. The T-matrix method is a forward problem algorithm, and later it was also used to solve inverse problems [26], [27]. In the T-matrix method, all field components are written in the form of multipole expansion. By matching the boundary conditions, the coefficients of the incident field and the scattered field are connected through the T-matrix [28].

First, we use LSM qualitative imaging method to get the approximate contour of the object to be reconstructed. Then take a point within the contour, and we regard a fixed radius circle centered at this point as the ''virtual experiment circle.'' By matching the boundary conditions on the virtual experiment circle, we can obtain a univariate equation about the media parameters at the sampling point. If we traverse all the sampling points inside the contour, we can get the media parameters in the entire target contour. In this way, we avoid matrix inversion, which further reduces the computational burden.

The structure of this article is as follows. In Section II, the structure of the inverse scattering imaging problem is described and the T-matrix method is reviewed. In Section III, the LSM qualitative imaging method and our new virtual experiment strategy are introduced. The simulation results and analysis are given in Section IV. Finally, the conclusion is drawn in Section V. Throughout this article, the time factor $e^{j\omega t}$ is adopted.

II. IMAGING STRUCTURE AND T-MATRIX METHOD

A. IMAGING STRUCTURE

We consider the incidence of TM waves in a two-dimensional plane, and its structure is shown in Fig. 1. The region D is embedded in a homogeneous and lossless background. We call the region D the imaging domain or the region of interest (ROI). Domain D contains one or more objects, the shape and electromagnetic parameters of which are unknown. The support of the target is Ω. The magnetic permeability is everywhere equal to that of free space μ_0. Define the contrast function of the target as $\chi(\boldsymbol{r}) = \varepsilon_r(\boldsymbol{r}) - 1$, where ε_r represents the complex relative permittivity. N_r receiving sensors are distributed on the curve Γ outside the imaging domain. Use plane waves to illuminate the imaging domain N_{inc} times from different directions, the scattered field at the location of N_r receiving points can be measured during each illumination, so we can get the data matrix of $N_r \times N_{inc}$. Inverse scattering imaging is to reconstruct the characteristics of the target through these data.

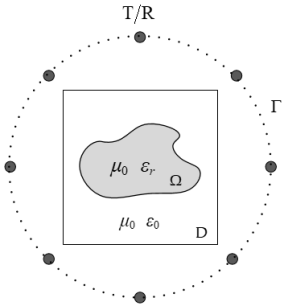

FIGURE 1. The configuration of the inverse scattering problem.

B. IMAGING FRAMEWORK BASED ON T-MATRIX METHOD

The T-matrix method first meshes the imaging domain D into N subunits, and then all the subunits are equivalent to equal-area circles, assuming that the radius of these equal-area circles is r_0. We assume that there is an infinite stretch of space in the direction perpendicular to the 2-D plane in Fig. 1, which maps circles on the plane to cylinders in the 3-D space. So the inverse scattering problem is transformed into reconstructing the medium parameters of these N small cylinders. In order to facilitate the description of the T-matrix method, we establish a multi-cylinder system as shown in Fig. 2. Under the global cylindrical coordinate system, the center coordinate of the ith cylinder is $\boldsymbol{\rho}_i = (r_{0,i}, \varphi_{0,i})$, $i = 1, 2, \cdots, N$.

Since the incident field is TM plane wave, the electric field only has a component in the z direction. Under the global coordinate system, the incident electric field at the observation point $\boldsymbol{r}$ can be expressed as

$$E_{zi}^{inc}(r, \varphi) = E_0 e^{jk_0 r\cos(\varphi - \varphi_0)}, \tag{1}$$

where φ_0 is the angle between the propagation direction of the incident wave and the negative x-axis, and $k_0 = \omega\sqrt{\mu_0\varepsilon_0}$ is the wavenumber in free space.

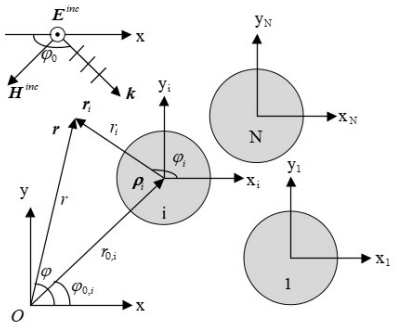

FIGURE 2. Geometry of multiple cylinders and coordinate systems.

Under the ith local cylindrical coordinate system with $\boldsymbol{\rho}_i = (r_{0,i}, \varphi_{0,i})$ as the origin, the incident electric field can be expressed as the form of multipole expansion

$$E_{zi}^{inc}(r_i, \varphi_i) = E_0 \sum_{m=-\infty}^{\infty} a_{im} J_m(k_0 r_i) e^{jm\varphi_i}, \quad i = 1, 2 \cdots, N \tag{2}$$

where J_m represents the mth order Bessel function of the first kind, $\boldsymbol{r}_i = (r_i, \varphi_i)$ is the coordinate of the observation point $\boldsymbol{r}$ under the ith local coordinate system, with $\boldsymbol{r}_i = \boldsymbol{r} - \rho_i$. And $a_{im} = e^{jk_0 r_{0,i} \cos(\varphi_{0,i} - \varphi_0)} j^m e^{-jm\varphi_0}$ is the coefficient of the multipole expansion, which can be easily derived from (1).

Under the ith local coordinate system, the scattered electric field corresponding to the ith cylinder is

$$E_{zi}^{s}(r_i, \varphi_i) = E_0 \sum_{m=-\infty}^{\infty} c_{im} H_m^{(2)}(k_0 r_i) e^{jm\varphi_i}, \quad i = 1, 2, \cdots, N \tag{3}$$

where $H_m^{(2)}$ is the mth order Hankel function of the second kind, c_{im} denotes the unknown expansion coefficient of the scattered electric field corresponding to the ith cylinder.

Inside the ith cylinder, the total electric field can be expressed as

$$E_{zi}^{tr}(r_i, \varphi_i) = E_0 \sum_{m=-\infty}^{\infty} b_{im} J_m(k_i r_i) e^{jm\varphi_i}, \quad i = 1, 2, \cdots, N \tag{4}$$

where b_{im} represents the unknown expansion coefficient. $k_i = k_0 \sqrt{\varepsilon_{ri} \mu_{ri}}$ denotes the wavenumber inside the ith cylinder, ε_{ri} and μ_{ri} represent the relative permittivity and relative permeability of the ith cylinder, respectively.

It can be derived from Maxwell's equations, the φ component of the magnetic field can be expressed as

$$H_{\varphi i} = \frac{1}{j\eta k} \frac{\partial E_{zi}}{\partial r_i}, \quad i = 1, 2, \cdots, N \tag{5}$$

where η and k represent the wave impedance and wavenumber in the corresponding medium, respectively.

On the surface of the ith cylinder, the boundary conditions of the electric and magnetic fields can be expressed as

$$E_{zi}^{inc} + \sum_{p=1}^{N} E_{zp}^{s} = E_{zi}^{tr}, \quad r_i = r_0, 0 \le \varphi_i \le 2\pi \tag{6}$$

$$H_{\varphi i}^{inc} + \sum_{p=1}^{N} H_{\varphi p}^{s} = H_{\varphi i}^{tr}, \quad r_i = r_0, 0 \le \varphi_i \le 2\pi \tag{7}$$

where the first term on the left side of the above two formulas is the incident field, and the right side is the total field. The second term on the left is the sum of the scattered fields of the N cylinders on the surface of the ith cylinder. It is worth noting that these N terms are all expressed in their respective local coordinate systems. Since in (2), (3) and (4), the expression of the fields has considered the multiple interactions between cylinders, so the fields in (6) and (7) include multiple scattering between cylinders. Using the addition theory of Hankel function [29], all scattered fields can be converted to the ith local coordinate system. After using the orthogonality of $e^{jm\varphi_i}$ to eliminate the total field in (6) and (7), the following formula can be obtained [28]

$$a_{il} = \sum_{p=1}^{N} \sum_{m=-M}^{M} c_{pm} \left[g_{ip}^{lm} (1 - \delta_{ip}) + d_{il} \delta_{lm} \delta_{ip} \right], \quad i = 1, 2, \cdots, N; l = -M, \cdots, M \tag{8}$$

where M is the truncation order of the multipole expansion. $\delta_{ip} = 1$ if $i = p$, other cases $\delta_{ip} = 0$. The expression of g_{ip}^{lm} and d_{il} can be found in literature [28].

For these N cylinders, each cylinder can get equations similar to (8), write them in the form of large matrix equations as follows

$$\boldsymbol{a} = (\boldsymbol{G} + \boldsymbol{O})\boldsymbol{c}, \tag{9}$$

where $\boldsymbol{a}$ and $\boldsymbol{c}$ are the vector form of a_{il} and c_{pm} in (8), respectively. $\boldsymbol{a}$ and $\boldsymbol{c}$ are both $N(2M+1) \times 1$ column vector, and they represent the unknown expansion coefficients in (2) and (3), respectively. $\boldsymbol{G}$ and $\boldsymbol{O}$ are square matrix of size $N(2M+1) \times N(2M+1)$, and they are the matrix form of g_{ip}^{lm} and d_{il} in (8). It is worth noting that $\boldsymbol{O}$ is a diagonal matrix.

By defining $\boldsymbol{T} = \boldsymbol{O}^{-1}$, we can easily get the following formula from (9)

$$\boldsymbol{T}(\boldsymbol{a} - \boldsymbol{G}\boldsymbol{c}) = \boldsymbol{c}. \tag{10}$$

The matrix $\boldsymbol{T}$ is also a diagonal matrix, and $\boldsymbol{T}$ is closely related to the media parameters of the N cylinders. If the matrix $\boldsymbol{T}$ is obtained, the media parameters of the N cylinders can be easily obtained from it. Therefore, the above framework is called the T-matrix method.

For N_r observation points on Γ, the scattered field at each observation point can be written as the superposition of the scattered fields contributed by the N cylinders, and this process can be expressed in the form of the following matrix equation

$$\boldsymbol{u}^{sca} = \boldsymbol{K}\boldsymbol{c}, \tag{11}$$

where $\boldsymbol{K}$ is a matrix of size $N_r \times N(2M+1)$. The elements K_{qi}^m of matrix $\boldsymbol{K}$ can be obtained from (3), and $K_{qi}^m = E_0 H_m^{(2)}(k_0 d_{iq}) e^{jm\varphi_{iq}}$, where d_{iq} is the distance between the center of the ith subunit and the qth observation point, and φ_{iq} is the azimuth angle from the center of the ith subunit to the qth observation point.

Equations (10) and (11) are the state equation and measurement equation of the T-matrix method. For the inverse scattering problem, $\boldsymbol{T}$ and $\boldsymbol{c}$ are the unknowns in the equations. The purpose of the inverse scattering problem is to obtain the T-matrix by solving these two equations, and further obtain the media parameters of all the subunits in the imaging domain.

III. APPLY VIRTUAL EXPERIMENT TO T-MATRIX SCHEME

A. LINEAR SAMPLING METHOD FOR QUALITATIVE IMAGING

LSM is a qualitative imaging method for reconstructing the shape of scatterers. The basic idea is to project the scattered field containing the target position information as the radiation field generated by a point source (line source in the two-dimensional case). This process can be expressed as

$$\int_\Gamma \xi(\varphi, \boldsymbol{r}_s) E^s(\boldsymbol{r}, \varphi) d\varphi = G(\boldsymbol{r}, \boldsymbol{r}_s), \quad \boldsymbol{r} \in \Gamma; \boldsymbol{r}_s \in D \quad (12)$$

where $\boldsymbol{r}_s$ is the sampling point, and $\xi(\varphi, \boldsymbol{r}_s)$ represents the weighting coefficient of the scattered field, which is a function of the location of the sampling point. $G(\boldsymbol{r}, \boldsymbol{r}_s)$ is the Green's function in the background medium, and φ represents the angle of the incident wave.

The left side of (12) is the form of continuous integration. In the actual measurement process, we illuminate the target N_{inc} times, and then (12) can be written into the following discrete form

$$\frac{2\pi}{N_{inc}} \sum_{t=1}^{N_{inc}} \xi(\varphi_t, \boldsymbol{r}_s) E^s(\boldsymbol{r}_m, \varphi_t) = -\frac{j}{4} H_0^{(2)}(k_0 |\boldsymbol{r}_m - \boldsymbol{r}_s|), \quad m = 1, 2, \cdots, N_r \quad (13)$$

where the subscript t denotes the tth illumination.

On the surface, the above process is a weighted superposition of the scattered fields of different illumination directions, but in fact, different weights are assigned to the illumination sources in different directions, and they are recombined to meet certain characteristics. Solving (13) we can get the weighting coefficient $\xi(\varphi, \boldsymbol{r}_s)$ of the sampling point $\boldsymbol{r}_s$. But (13) is ill-posed and needs to be dealt with by regularization strategy, here the Tikhonov regularization strategy is used. If we sample sequentially at the center point of all subunits, the weighting coefficient of the entire imaging domain can be obtained. After obtaining these weighting coefficients, we use the formula given in the literature [23] as the indicator function

$$\Upsilon(\boldsymbol{r}_s) = \frac{\log_{10} \|\xi_s\| - \log_{10} \|\xi_s\|_{\max}}{\min\left[\log_{10} \|\xi_s\| - \log_{10} \|\xi_s\|_{\max}\right]}, \quad s = 1, 2, \cdots, N \quad (14)$$

where $\|\cdot\|$ represents the 2-norm of a vector. Υ is the indicator function of target's support, and those points whose indicator function value is close to 1 belong to the target area. Therefore, we can set a threshold Ψ and consider that the sampling points with an indicator function value greater than Ψ belong to the target area. In this way, the target's contour can be obtained.

B. NEW VIRTUAL EXPERIMENTS STRATEGY

After the weighting coefficients of all sampling points are obtained, for the boundary conditions in (6) and (7), the field components on both sides of the equation can be multiplied by the same coefficient, and the following equation can be obtained

$$\begin{aligned} &\frac{2\pi}{N_{inc}} \sum_{t=1}^{N_{inc}} \xi(\varphi_t, \boldsymbol{r}_s) E_{zi}^{inc}(\boldsymbol{r}_i, \varphi_t) + \frac{2\pi}{N_{inc}} \sum_{t=1}^{N_{inc}} \xi(\varphi_t, \boldsymbol{r}_s) \\ &\quad \times \sum_{p=1}^{N} E_{zp}^s(\boldsymbol{r}_i, \varphi_t) \\ &= \frac{2\pi}{N_{inc}} \sum_{t=1}^{N_{inc}} \xi(\varphi_t, \boldsymbol{r}_s) E_{zi}^{tr}(\boldsymbol{r}_i, \varphi_t), \end{aligned} \quad (15)$$

$$\begin{aligned} &\frac{2\pi}{N_{inc}} \sum_{t=1}^{N_{inc}} \xi(\varphi_t, \boldsymbol{r}_s) H_{\varphi i}^{inc}(\boldsymbol{r}_i, \varphi_t) + \frac{2\pi}{N_{inc}} \sum_{t=1}^{N_{inc}} \xi(\varphi_t, \boldsymbol{r}_s) \\ &\quad \times \sum_{p=1}^{N} H_{\varphi p}^s(\boldsymbol{r}_i, \varphi_t) \\ &= \frac{2\pi}{N_{inc}} \sum_{t=1}^{N_{inc}} \xi(\varphi_t, \boldsymbol{r}_s) H_{\varphi i}^{tr}(\boldsymbol{r}_i, \varphi_t). \end{aligned} \quad (16)$$

As shown in Fig. 3, $\boldsymbol{r}_s$ is the sampling point within the target's contour. $\boldsymbol{r}_i$ is located on the circle centered on the center of the ith subunit, and we call this circle the virtual experiment circle. Note that (15) and (16) are established under the assumption that the target's medium parameters are uniform in the virtual experimental circle.

In the T-matrix method, $\boldsymbol{r}_i$ is located on the circumference of equal-area circle which equivalent to the meshed subunit. As long as the mesh is determined, the position of $\boldsymbol{r}_i$ is determined. In our proposed method, $\boldsymbol{r}_i$ is located on the virtual experiment circle, but the virtual experiment circle is no longer restricted by the mesh. The radius of the virtual experiment circle, that is, R_i, may not be equal to the radius of the equal-area circle. R_i is adjusted according to the size of the target contour, so the choice of R_i is flexible. We will elaborate on the choice of R_i later.

The basic Equation (12) of LSM was originally established outside the imaging domain. Here we make an approximation and think that this equation holds in the imaging domain. In fact, the classic LSM quantitative imaging method does the same [21]. Therefore, the rearranged scattered field in (15) and (16) can be replaced by the right side of (13).

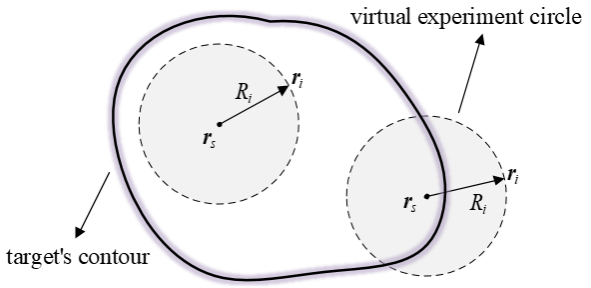

FIGURE 3. Schematic diagram of virtual experiment circles.

If we force the sampling point $\boldsymbol{r}_s$ to coincide with the center of the ith subunit, then (15) and (16) can be written as follows

$$\frac{2\pi}{N_{inc}}\sum_{t=1}^{N_{inc}}\xi(\varphi_t,\boldsymbol{r}_s)E_{zi}^{inc}(\boldsymbol{r}_i,\varphi_t)+\left[-\frac{j}{4}H_0^{(2)}(k_0r_i)\right]$$
$$=\frac{2\pi}{N_{inc}}\sum_{t=1}^{N_{inc}}\xi(\varphi_t,\boldsymbol{r}_s)E_{zi}^{tr}(\boldsymbol{r}_i,\varphi_t),\quad r_i=R_i,0\le\varphi_i\le 2\pi \tag{17}$$

$$\frac{2\pi}{N_{inc}}\sum_{t=1}^{N_{inc}}\xi(\varphi_t,\boldsymbol{r}_s)H_{\varphi i}^{inc}(\boldsymbol{r}_i,\varphi_t)+\frac{1}{j\eta_0k_0}\frac{\partial}{\partial r_i}\left[-\frac{j}{4}H_0^{(2)}(k_0r_i)\right]$$
$$=\frac{2\pi}{N_{inc}}\sum_{t=1}^{N_{inc}}\xi(\varphi_t,\boldsymbol{r}_s)H_{\varphi i}^{tr}(\boldsymbol{r}_i,\varphi_t),\quad r_i=R_i,0\le\varphi_i\le 2\pi \tag{18}$$

where $\eta_0=\sqrt{\mu_0/\varepsilon_0}$ is wave impedance in the free space, and R_i represents the radius of the virtual experiment circles. Equations (17) and (18) are derived by matching boundary conditions and are valid in $\boldsymbol{r}_i$, so they are different from the approach in [21] wherein the basic equation holds true in all the point of the imaging domain. This implies that: a) the field approximation has a wider range of validity, b) there is no need of filtering the Hankel function, and c) the virtual circle probably implies an average operation which deletes possible inaccuracies.

Considering the influence of R_i on the inversion results, we must choose R_i carefully. In Equations (17) and (18), according to the framework of the T-matrix method, we assume that the parameters inside the virtual experiment circle are uniform. Therefore, when R_i is too large, the media parameters of subunits close to each other will tend to be consistent. In addition, for sampling points located near the edge of the target's contour, a large R_i will cause the virtual experimental circle to contain too many non-target areas, resulting in inaccurate imaging results. On the other hand, the value of R_i cannot be too small. Because when R_i approaches zero, the Hankel function term on the left of (17) and (18) will tend to a singular value, which will increase the approximate error of the rearranged scattered field. After a lot of experiments, our experience is that when the value of R_i is close to the size of the truncated target region, the error of the second term in (17) and (18) is small, and the inversion accuracy can be take into account, although there is no strict proof.

After simplifying (17) and (18), the following equation can be obtained. The specific calculation process is given in the Appendix.

$$\frac{2\pi}{N_{inc}}\sum_{t=1}^{N_{inc}}\xi(\varphi_t,\boldsymbol{r}_s)e^{jk_0r_{0,i}\cos(\varphi_{0,i}-\varphi_t)}$$
$$=\frac{j}{4}+\frac{1}{4}\frac{\eta_{ri}J_0(k_iR_i)Y_1(k_0R_i)-J_1(k_iR_i)Y_0(k_0R_i)}{\eta_{ri}J_0(k_iR_i)J_1(k_0R_i)-J_0(k_0R_i)J_1(k_iR_i)} \tag{19}$$

where Y_0 and Y_1 represent the 0th and 1st order Bessel functions of the second kind, respectively. $\eta_{ri}=\sqrt{1/\varepsilon_{ri}}$ and $k_i=\sqrt{\varepsilon_{ri}}k_0$ respectively represent the relative wave impedance and wavenumber of the ith virtual experiment circle. From Equation (19), we know that for a fixed radius R_i, the right side is only the function of relative permittivity. Since the left side of (19) is known, we can solve it to get the relative permittivity. But the right side of (19) is nonlinear, so it is not easy to solve it directly. In order to study the characteristics on the right side of (19), we let

$$f(\varepsilon_{ri})=\frac{j}{4}+\frac{1}{4}\frac{\eta_{ri}J_0(k_iR_i)Y_1(k_0R_i)-J_1(k_iR_i)Y_0(k_0R_i)}{\eta_{ri}J_0(k_iR_i)J_1(k_0R_i)-J_0(k_0R_i)J_1(k_iR_i)}. \tag{20}$$

Fig. 4 shows the curve of $\mathrm{Re}[f(\varepsilon_{ri})]$ when R_i takes different values. It can be seen from the figure that no matter how much the value of R_i is taken, $\mathrm{Re}[f(\varepsilon_{ri})]$ is monotonic. Therefore, as long as the left side of (20) is obtained, the value of relative permittivity can be uniquely determined. What's more, because the curve of $\mathrm{Re}[f(\varepsilon_{ri})]$ changes slowly, a small change of $\mathrm{Re}[f(\varepsilon_{ri})]$ will cause a large difference in ε_{ri}. This requires that the error on the left side of (20) cannot be too large, otherwise the reconstruction error will be relatively large. It is worth noting that we only considered the case

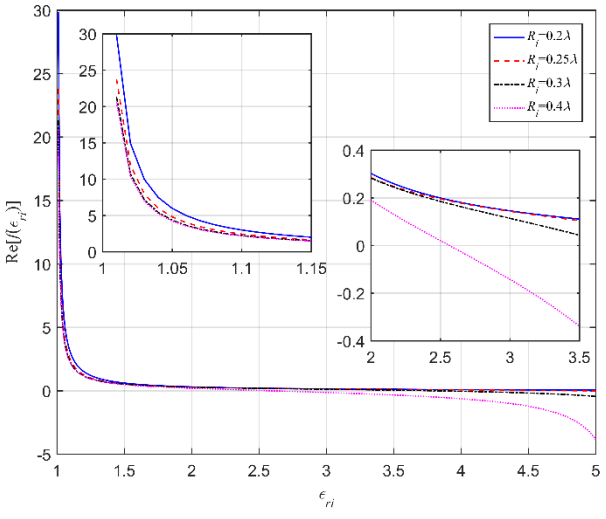

FIGURE 4. The change curve of the real part of function f with ε_{ri}.

where ε_{ri} is real. If ε_{ri} is a complex value, that is, the material of the target is a lossy medium, then (20) is a binary function.

After obtaining the left side of (20), we select an appropriate R_i according to the size of the truncated area, and the ε_{ri} of this subunit can be obtained by means of the look-up table method. By sequentially selecting each subunit center in the truncated area as the sampling point, the relative permittivity distribution in the target area can be obtained. Compared with the LSM quantitative imaging method, we avoid solving the linear system of equations, which greatly improves the computational efficiency.

The proposed method has some things in common with [21] and [22]. The proposed method and [21] adopt a similar total field approximation in the imaging area, which simplifies the problem. Literature [22] assumes that the contrast changes slowly around each pivot point, and we assume that the target is uniform within virtual experimental circles. In addition, the proposed method and [22] both use algebraic methods to solve the contrast.

IV. NUMERICAL SIMULATIONS

A. SIMULATION CONDITIONS

We use simulation data to verify the effectiveness of the proposed method, and compare it with the LSM quantitative imaging method and the CSI method. In order to avoid inverse crime, the measurement data is generated by the CG-FFT method [30], [31] and is contaminated by Gaussian noise with $SNR = 20dB$. The range of the domain D is $2\lambda_b \times 2\lambda_b$, where λ_b is the wavelength in the background medium. According to the principle of freedom degree in the literature [32], we take the number of incident waves $N_{inc} = 20$, the number of receiving points N_r is also 20, and the receiving sensors are evenly distributed on a circle with a radius of $3\lambda_b$. For the selection of the LSM truncation threshold, we uniformly take $\Psi = 0.5$. After a lot of experiments, we believe that this is a reasonable choice.

For the reconstruction results of the LSM quantitative imaging method given in Section IV B, we used the method mentioned in [21] to deal with the singularity of $H_0^{(2)}$, and performed low-pass filtering on $H_0^{(2)}$. When solving ill-posed linear equations, Tikhonov regularization strategy is adopted. In order to compare the reconstruction accuracy of different algorithms, we define the reconstruction error as shown in the following formula

$$err = \frac{\sum_{i=1}^{N} \|\chi_i - \widetilde{\chi}_i\|^2}{\sum_{i=1}^{N} \|\chi_i\|^2}, \tag{21}$$

where $\widetilde{\chi}_i$ is the estimated contrast of the ith subunit and χ_i the actual one.

In fact, it is unfair to compare the reconstruction errors between the proposed method and LSM quantitative imaging method. Because the contour information of the target is exploited to calculate the reconstruction error of the proposed method, while the whole imaging area is considered when calculating the reconstruction error of the LSM quantitative imaging method. Even so, using (21) to define the reconstruction error of the proposed method still has reference value.

B. EXAMPLES

Example 1: The first example is a circler object as shown in Fig. 5(a), whose radius is $0.5\lambda_b$. The relative permittivity is $\varepsilon_r = 2.5$, then the electrical size of this target is $1.58\lambda_b$. For this example, the entire imaging domain is meshed into a 40×40 grid. We first exploit LSM to estimate the target geometry, the indicator map is shown in Fig. 5(b). According to the contour obtained by truncating the LSM indicator function, we take $R_i = 0.4\lambda_b$ as the radius of the virtual experiment circle. Fig. 5(c) shows the reconstruction result of the proposed method, from which we can see that the target has been basically restored. In order to compare the performance of the algorithm, we also used the LSM quantitative imaging method to reconstruct the object. Fig. 5(d) shows the pivot points in LSM quantitative method. In Fig. 5(e), we give the reconstruction result of the LSM quantitative imaging method.

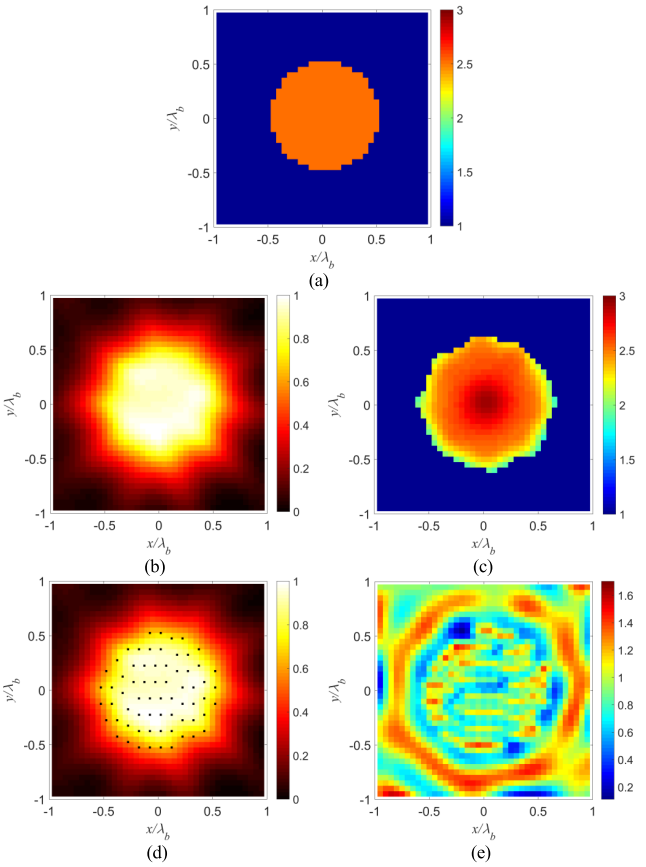

FIGURE 5. Single cylinder target. (a) Original pattern. (b) Normalized logarithmic LSM indicator map. (c) Reconstruction pattern by the proposed method. (d) The selected pivot points in LSM quantitative imaging method. (e) Reconstruction pattern by LSM quantitative imaging method.

The reconstruction error of the proposed method is $err = 31.8\%$, and the reconstruction error of the LSM quantitative imaging method is $err = 129\%$. Since the electrical size

of this target exceeds $1.22\lambda_b$, it cannot be reconstructed by the LSM quantitative imaging method, which confirms the conclusion in literature [24]. Compared with the classic LSM quantitative imaging method, the proposed method breaks this limitation and successfully reconstructs the target. The proposed method has wider applicability, possibly because we assume that the target is uniform in the virtual experiment circles, which provides strong prior information and has a positive effect on the reconstruction of the target.

Example 2: The second example deals with two square scatterers. As shown in Fig. 6(a), the side length of the square column is $0.5\lambda_b$, and the relative permittivity of these two objects is $\varepsilon_r = 2.0$. The meshing is the same as the previous example. According to the target contour obtained by truncating the indicator function shown in Fig. 6(b), the virtual experiment circle radius is $R_i = 0.3\lambda_b$. Fig. 6(c) is the reconstruction result by the proposed approach, and the reconstruction error is $err = 10.4\%$. Fig. 6(d) and Fig. 6(e) are the images in LSM quantitative imaging. It can be seen from the reconstruction results that both the proposed method and the LSM quantitative imaging method have successfully reconstructed the target position and media parameters. In this example, the reconstruction error of the LSM quantitative method is $err = 14.5\%$.

Example 3: Fig. 7(a) shows the third example: a ring and two circular objects. The inner and outer radii of the ring are $0.3\lambda_b$ and $0.5\lambda_b$, respectively, and the radii of the two small circles are $0.15\lambda_b$. The relative permittivity of the ring is $\varepsilon_r = 1.5$, and $\varepsilon_r = 2.0$ of the cylinders'. For this example, the imaging domain is meshed into a 60×60 grid. The reason for this is to study the influence of the number of unknowns on the calculation time, which is analyzed in detail in the next section. Consistent with the analysis in the previous section, the radius of the virtual experiment circle is $R_i = 0.2\lambda_b$. It can be seen from Fig. 7(c) and 7(e) that both the proposed method and the LSM method successfully restore the target. The reconstruction errors of the proposed method and the LSM quantitative imaging method are $err = 27.7\%$ and $err = 23.8\%$, respectively. It is worth noting that the distance between the targets given in this example is smaller than the wavelength, but the proposed method successfully reconstructs the targets, which shows the proposed method has a certain resolution ability.

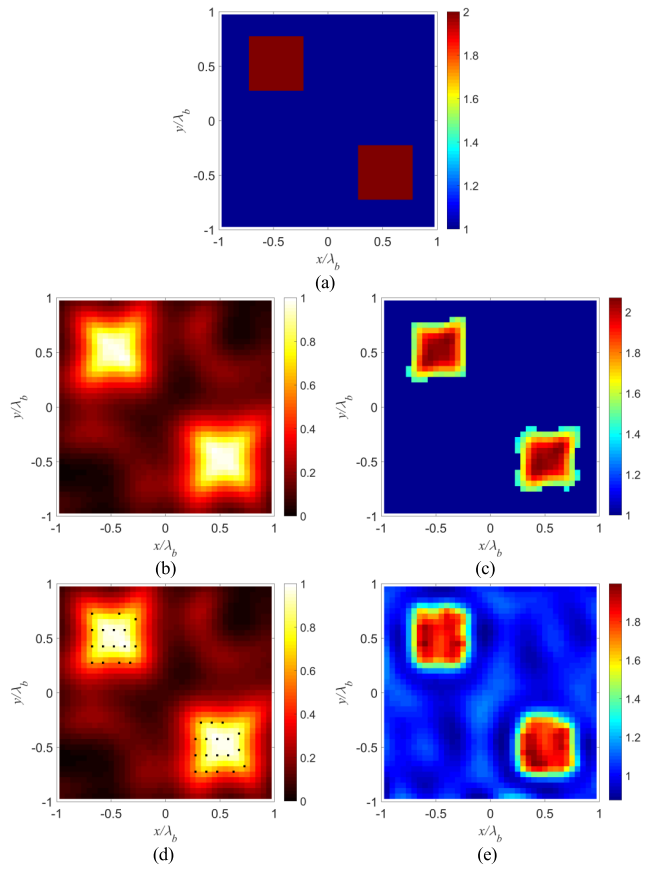

FIGURE 6. Two square objects. (a) Original pattern. (b) Normalized logarithmic LSM indicator map. (c) Reconstruction pattern by the proposed method. (d) The selected pivot points in LSM quantitative imaging method. (e) Reconstruction pattern by LSM quantitative imaging method.

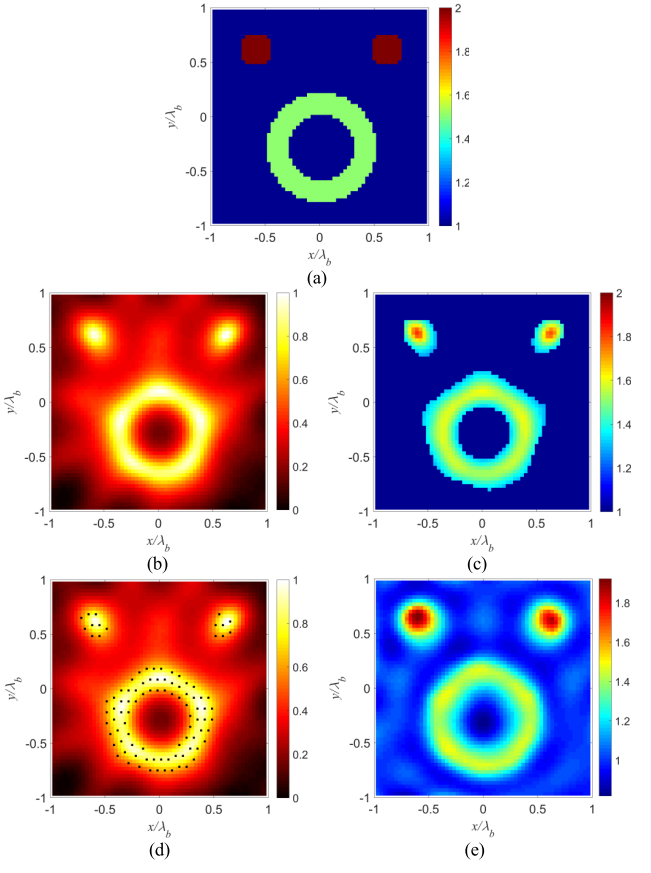

FIGURE 7. A ring and two circular objects. (a) Original pattern. (b) Normalized logarithmic LSM indicator map. (c) Reconstruction pattern by the proposed method. (d) The selected pivot points in LSM quantitative imaging method. (e) Reconstruction pattern by LSM quantitative imaging method.

Example 4: In the fourth example, we have three circular objects with different radii as shown in Fig. 8(a). Their radii are $0.15\lambda_b$, $0.2\lambda_b$ and $0.25\lambda_b$, and the corresponding relative permittivity is $\varepsilon_r = 3.5$, 3.0 and 2.5 respectively. Fig. 8(b) is the LSM indicator map and Fig. 8(c) is the reconstruction result by the proposed method. Since the contour sizes obtained by the truncation of the three objects are different, we choose a compromised virtual experimental circle radius, and we take $R_i = 0.25\lambda_b$. Meanwhile, we also use CSI method to reconstruct this example. Fig. 8(d) is the reconstruction result of CSI method after 200 iterations. The contrast reconstruction error of the proposed method and CSI method are $err = 21.98\%$ and $err = 14.65\%$, respectively. The reconstruction result of the CSI method has higher accuracy, but also has a heavier computational burden.

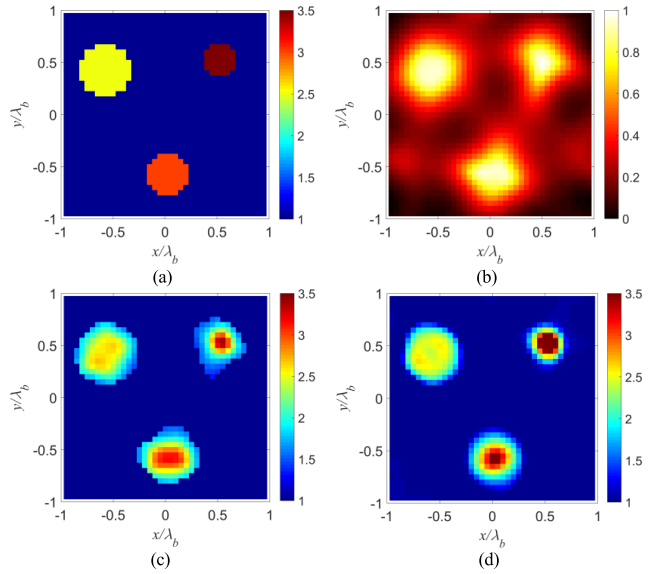

FIGURE 8. Three circular objects with different sizes. (a) Original pattern. (b) Normalized logarithmic LSM indicator map. (c) Reconstruction pattern by the proposed method. (d) Reconstruction pattern of 200 iterations with CSI method.

The proposed method assumes that the target is uniform within virtual experimental circles, so it is difficult to reconstruct complex targets, because for objects with complex shapes, this assumption is difficult to hold. It can be seen from the results of the above several examples that the reconstructed relative permittivity is more accurate in the position close to the center of the target. At the edge of the target, the reconstruction error of the contrast is larger. This is because the proposed method assumes that the medium inside the virtual experiment circle is uniform. Therefore, for the sampling points near the edge of the target contour, the reconstructed relative permittivity value contains a part of the contribution of the non-target area, as shown in Fig. 3, so the result is not accurate.

C. COMPUTATIONAL TIME

The proposed method has no iterative process and do not contain the process of solving linear system of equations. It only needs to solve a series of univariate equations by the look-up table method. The computational complexity of the LSM qualitative imaging method is related to the size of the antenna array. Classical LSM quantitative imaging method requires solving a system of linear equations with N variables, where N is the number of the meshed subunits. In each iteration step of CSI method, the computational complexity of conjugate gradient method is $O(N \log N)$.

Table 1 shows the calculation time of several examples in the previous section (Xeon(R) CPU, 2.40GHz). Among them, the number of iterative steps of the CSI method in *Example 4* is 200 steps. Note that the calculation time here does not include the time to generate measurement data using the forward algorithm. The calculation time of the LSM quantitative imaging method includes two parts: the time of LSM qualitative imaging and the time of solving linear equations. The calculation time of the proposed method includes the time of LSM qualitative imaging and the time of solving a series of unary equations. Compared with the LSM quantitative imaging method, the proposed method has higher computational efficiency. It can be seen from the table that the calculation time of the proposed method is an order of magnitude faster than that of the CSI method. Even if the calculation accuracy is not as good as the CSI method, considering the substantial increase in calculation efficiency, we think our work is meaningful.

TABLE 1. The computational times.

	The proposed method	LSM quantitative imaging method	CSI method
Example 1	1.21s	3.49s	-
Example 2	1.23s	2.86s	-
Example 3	1.59s	8.78s	-
Example 4	1.25s	-	77.49s

V. CONCLUSION

We propose a fast method for reconstructing dielectric objects, which does not even need to solve linear equation system. First, we use the LSM qualitative imaging method to obtain the contour of the target. Then we innovatively apply the preprocessing information of LSM to the boundary conditions of the T-matrix method. By transforming the parameter inversion problem into solving a series of univariate equations, the calculation efficiency is greatly improved. In terms of calculation time, the advantage of this method is huge. Through simulation experiments, we verified that the efficiency of the proposed algorithm is higher than that of the LSM quantitative imaging method, and the application range is also larger. The disadvantage of this method is that we only study the case of lossless media. In the next step, we will study the possibility of using the proposed method to solve reconstruction problem of lossy media and even metal objects.

APPENDIX

Below we give the derivation of (19). First, we write (17) and (18) below.

$$\frac{2\pi}{N_{inc}}\sum_{t=1}^{N_{inc}}\xi(\varphi_t,\boldsymbol{r}_s)E_{zi}^{inc}(\boldsymbol{r}_i,\varphi_t)+\left[-\frac{j}{4}H_0^{(2)}(k_0r_i)\right]=\frac{2\pi}{N_{inc}}\sum_{t=1}^{N_{inc}}\xi(\varphi_t,\boldsymbol{r}_s)E_{zi}^{tr}(\boldsymbol{r}_i,\varphi_t),\quad r_i=R_i,0\le\varphi_i\le 2\pi \tag{A1}$$

$$\frac{2\pi}{N_{inc}}\sum_{t=1}^{N_{inc}}\xi(\varphi_t,\boldsymbol{r}_s)H_{\varphi i}^{inc}(\boldsymbol{r}_i,\varphi_t)+\frac{1}{j\eta_0k_0}\frac{\partial}{\partial r_i}\left[-\frac{j}{4}H_0^{(2)}(k_0r_i)\right]=\frac{2\pi}{N_{inc}}\sum_{t=1}^{N_{inc}}\xi(\varphi_t,\boldsymbol{r}_s)H_{\varphi i}^{tr}(\boldsymbol{r}_i,\varphi_t),\quad r_i=R_i,0\le\varphi_i\le 2\pi \tag{A2}$$

Substituting (2) and (4) into the above two formulas, and using (5) to calculate the magnetic field component, the following two formulas are obtained.

$$\frac{2\pi}{N_{inc}}\sum_{t=1}^{N_{inc}}\xi(\varphi_t,\boldsymbol{r}_s)\sum_{m=-\infty}^{\infty}e^{jk_0r_{0,i}\cos(\varphi_{0,i}-\varphi_t)}j^me^{-jm\varphi_t}\times J_m(k_0R_i)e^{jm\varphi_i}+\left[-\frac{j}{4}H_0^{(2)}(k_0R_i)\right]=\frac{2\pi}{N_{inc}}\sum_{t=1}^{N_{inc}}\xi(\varphi_t,\boldsymbol{r}_s)\times\sum_{m=-\infty}^{\infty}b_{im}^tJ_m(k_iR_i)e^{jm\varphi_i} \tag{A3}$$

$$\frac{2\pi}{N_{inc}}\sum_{t=1}^{N_{inc}}\xi(\varphi_t,\boldsymbol{r}_s)\sum_{m=-\infty}^{\infty}\frac{1}{j\eta_0}e^{jk_0r_{0,i}\cos(\varphi_{0,i}-\varphi_t)}j^me^{-jm\varphi_t}\times J_m'(k_0R_i)e^{jm\varphi_i}+\frac{1}{j\eta_0}\left[-\frac{j}{4}H_0^{(2)\prime}(k_0R_i)\right]=\frac{2\pi}{N_{inc}}\sum_{t=1}^{N_{inc}}\xi(\varphi_t,\boldsymbol{r}_s)\times\sum_{m=-\infty}^{\infty}\frac{1}{j\eta_i}b_{im}^tJ_m'(k_iR_i)e^{jm\varphi_i} \tag{A4}$$

Integrating φ_i from 0 to 2π on both sides of (A3) and (A4) simultaneously, which can remove all alternating components, and then we can get

$$\frac{2\pi}{N_{inc}}\sum_{t=1}^{N_{inc}}\xi(\varphi_t,\boldsymbol{r}_s)e^{jk_0r_{0,i}\cos(\varphi_{0,i}-\varphi_t)}J_0(k_0R_i)-\frac{j}{4}H_0^{(2)}(k_0R_i)=\frac{2\pi}{N_{inc}}\sum_{t=1}^{N_{inc}}\xi(\varphi_t,\boldsymbol{r}_s)b_{i0}^tJ_0(k_iR_i) \tag{A5}$$

$$\frac{2\pi}{N_{inc}}\sum_{t=1}^{N_{inc}}\xi(\varphi_t,\boldsymbol{r}_s)e^{jk_0r_{0,i}\cos(\varphi_{0,i}-\varphi_t)}J_0'(k_0R_i)-\frac{j}{4}H_0^{(2)\prime}(k_0R_i)=\frac{2\pi}{N_{inc}}\sum_{t=1}^{N_{inc}}\xi(\varphi_t,\boldsymbol{r}_s)\frac{\eta_0}{\eta_i}b_{i0}^tJ_0'(k_iR_i) \tag{A6}$$

Multiply (A5) by $\frac{\eta_0}{\eta_i}\frac{J_0'(k_iR_i)}{J_0(k_iR_i)}$, and then subtract (A6). After transformation, the following formula can be obtained

$$\frac{2\pi}{N_{inc}}\sum_{t=1}^{N_{inc}}\xi(\varphi_t,\boldsymbol{r}_s)e^{jk_0r_{0,i}\cos(\varphi_{0,i}-\varphi_t)}=-\frac{j}{4}\frac{\eta_iJ_0(k_iR_i)H_0^{(2)\prime}(k_0R_i)-\eta_0J_0'(k_iR_i)H_0^{(2)}(k_0R_i)}{\eta_0J_0'(k_iR_i)J_0(k_0R_i)-\eta_iJ_0(k_iR_i)J_0'(k_0R_i)} \tag{A7}$$

According to the equation relationship of the Bessel function, the right side of (A7) can be transformed into a function about the first and second types of Bessel functions:

$$\frac{2\pi}{N_{inc}}\sum_{t=1}^{N_{inc}}\xi(\varphi_t,\boldsymbol{r}_s)e^{jk_0r_{0,i}\cos(\varphi_{0,i}-\varphi_t)}=\frac{j}{4}+\frac{1}{4}\frac{\eta_{ri}J_0(k_iR_i)Y_1(k_0R_i)-J_1(k_iR_i)Y_0(k_0R_i)}{\eta_{ri}J_0(k_iR_i)J_1(k_0R_i)-J_0(k_0R_i)J_1(k_iR_i)} \tag{A8}$$

where $\eta_{ri}=\eta_i/\eta_0$ is the relative wave impedance inside the virtual experiment circle. J and Y represent the first and second type Bessel functions, respectively.

REFERENCES

[1] E. C. Fear, X. Li, S. C. Hagness, and M. A. Stuchly, "Confocal microwave imaging for breast cancer detection: Localization of tumors in three dimensions," *IEEE Trans. Biomed. Eng.*, vol. 49, no. 8, pp. 812–822, Aug. 2002.
[2] Ž. Bugarinović, L. Pajewski, A. Ristić, M. Vrtunski, M. Govedarica, and M. Borisov, "On the introduction of canny operator in an advanced imaging algorithm for real-time detection of hyperbolas in ground-penetrating radar data," *Electronics*, vol. 9, no. 3, p. 541, Mar. 2020.
[3] Z. Li and Z. Meng, "A review of the radio frequency non-destructive testing for carbon-fibre composites," *Meas. Sci. Rev.*, vol. 16, no. 2, pp. 68–76, Apr. 2016.
[4] S. Sun, B. J. Kooij, and A. G. Yarovoy, "Linearized 3-D electromagnetic contrast source inversion and its applications to half-space configurations," *IEEE Trans. Geosci. Remote Sens.*, vol. 55, no. 6, pp. 3475–3487, Jun. 2017.
[5] D. Colton and R. Kress, *Inverse Acoustic and Electromagnetic Scattering Theory*. Berlin, Germany: Springer-Verlag, 1992.
[6] W. H. Carter, "Inverse scattering in the first born approximation," *Opt. Eng.*, vol. 23, no. 2, pp. 204–209, Apr. 1984.
[7] A. Devaney, "A filtered backpropagation algorithm for diffraction tomography," *Ultrason. Imag.*, vol. 4, no. 4, pp. 336–350, Oct. 1982.
[8] Y. M. Wang and W. C. Chew, "An iterative solution of the two-dimensional electromagnetic inverse scattering problem," *Int. J. Imag. Syst. Technol.*, vol. 1, no. 1, pp. 100–108, 1989.
[9] W. C. Chew and Y. M. Wang, "Reconstruction of two-dimensional permittivity distribution using the distorted born iterative method," *IEEE Trans. Med. Imag.*, vol. 9, no. 2, pp. 218–225, Jun. 1990.
[10] M. Slaney, A. C. Kak, and L. E. Larsen, "Limitations of imaging with first-order diffraction tomography," *IEEE Trans. Microw. Theory Techn.*, vol. MTT-32, no. 8, pp. 860–874, Aug. 1984.
[11] R. E. Kleinman and P. M. van den Berg, "A modified gradient method for two-dimensional problems in tomography," *J. Comput. Appl. Math.*, vol. 42, no. 1, pp. 17–35, 1992.
[12] P. M. V. D. Berg and R. E. Kleinman, "A contrast source inversion method," *Inverse Problems*, vol. 13, no. 6, pp. 1607–1620, Dec. 1997.
[13] P. M. V. D. Berg, A. L. V. Broekhoven, and A. Abubakar, "Extended contrast source inversion," *Inverse Problems*, vol. 15, no. 5, pp. 1325–1344, Oct. 1999.
[14] X. Chen, "Subspace-based optimization method for solving inverse-scattering problems," *IEEE Trans. Geosci. Remote Sens.*, vol. 48, no. 1, pp. 42–49, Jan. 2010.
[15] T. Isernia, V. Pascazio, and R. Pierri, "A nonlinear estimation method in tomographic imaging," *IEEE Trans. Geosci. Remote Sens.*, vol. 35, no. 4, pp. 910–923, Jul. 1997.

[16] D. Colton and A. Kirsch, "A simple method for solving inverse scattering problems in the resonance region," *Inverse Problems*, vol. 12, no. 4, pp. 383–393, Aug. 1996.
[17] D. Colton, M. Piana, and R. Potthast, "A simple method using Morozov's discrepancy principle for solving inverse scattering problems," *Inverse Problems*, vol. 13, no. 6, pp. 1477–1493, Dec. 1997.
[18] D. Colton, H. Haddar, and M. Piana, "The linear sampling method in inverse electromagnetic scattering theory," *Inverse Problems*, vol. 19, no. 6, pp. S105–S137, Dec. 2003.
[19] L. Crocco, L. Di Donato, I. Catapano, and T. Isernia, "An improved simple method for imaging the shape of complex targets," *IEEE Trans. Antennas Propag.*, vol. 61, no. 2, pp. 843–851, Feb. 2013.
[20] L. Crocco, L. Di Donato, I. Catapano, and T. Isernia, "The factorization method for virtual experiments based quantitative inverse scattering," *Prog. Electromagn. Res.*, vol. 157, pp. 121–131, 2016.
[21] L. Crocco, I. Catapano, L. Di Donato, and T. Isernia, "The linear sampling method as a way to quantitative inverse scattering," *IEEE Trans. Antennas Propag.*, vol. 60, no. 4, pp. 1844–1853, Apr. 2012.
[22] M. T. Bevacqua, L. Crocco, L. Di Donato, and T. Isernia, "An algebraic solution method for nonlinear inverse scattering," *IEEE Trans. Antennas Propag.*, vol. 63, no. 2, pp. 601–610, Feb. 2015.
[23] L. Di Donato, M. T. Bevacqua, L. Crocco, and T. Isernia, "Inverse scattering via virtual experiments and contrast source regularization," *IEEE Trans. Antennas Propag.*, vol. 63, no. 4, pp. 1669–1677, Apr. 2015.
[24] L. Di Donato, R. Palmeri, G. Sorbello, T. Isernia, and L. Crocco, "Assessing the capabilities of a new linear inversion method for quantitative microwave imaging," *Int. J. Antennas Propag.*, vol. 2015, Jun. 2015, Art. no. 403760.
[25] P. C. Waterman, "Matrix formulation of electromagnetic scattering," *Proc. IEEE*, vol. 53, no. 8, pp. 805–811, Aug. 1965.
[26] X. Ye, X. Chen, Y. Zhong, and R. Song, "Simultaneous reconstruction of dielectric and perfectly conducting scatterers via T-matrix method," *IEEE Trans. Antennas Propag.*, vol. 61, no. 7, pp. 3774–3781, Jul. 2013.
[27] Y. Gan, C. Yin, Q. Fan, and A. Li, "Improved T-Matrix method for simultaneous reconstruction of dielectric and perfectly conducting scatterers," *IEEE Access*, vol. 8, pp. 143622–143631, 2020.
[28] A. Z. Elsherbeni and A. A. Kishk, "Modeling of cylindrical objects by circular dielectric and conducting cylinders," *IEEE Trans. Antennas Propag.*, vol. 40, no. 1, pp. 96–99, Jan. 1992.
[29] W. C. Chew, *Waves and Fields in Inhomogeneous Media*, 2nd ed. New York, NY, USA: IEEE Press, 1995.
[30] C. Y. Shen, K. J. Glover, M. I. Sancer, and A. D. Varvatsis, "The discrete Fourier transform method of solving differential-integral equations in scattering theory," *IEEE Trans. Antennas Propag.*, vol. 37, no. 8, pp. 1032–1041, Aug. 1989.
[31] K. Barkeshli and J. L. Volakis, "On the implementation of the conjugate gradient Fourier transform method for scattering by planar plates," *IEEE Antennas Propag. Mag.*, vol. 32, no. 2, pp. 20–26, Apr. 1990.
[32] O. M. Bucci and T. Isernia, "Electromagnetic inverse scattering: Retrievable information and measurement strategies," *Radio Sci.*, vol. 32, no. 6, pp. 2123–2137, Nov. 1997.

YONGJI GAN received the B.S. degree in electronic science and technology from the School of Electronic and Information Engineering, South China University of Technology, Guangzhou, China, in 2018. He is currently pursuing the M.S. degree in information and communication engineering with the National University of Defense Technology.

His research interests include inverse scattering problems and imaging technology.

CHENGYOU YIN received the M.S. degree in electromagnetic field and microwave technology from the Institute of Electronics Engineering, Hefei, China, and the Ph.D. degree in electrical and computer engineering from the University of Science and Technology, Hefei.

He is currently a Professor with the National University of Defense Technology. His main research interests include computational electromagnetics, inverse scattering, and data fusion.

QIMENG FAN received the B.S. and M.S. degrees in electromagnetic field and microwave technology, and the Ph.D. degree in information and communication engineering from the College of Electronics Engineering, National University of Defense Technology, Hefei, China, in 2014, 2016, and 2019, respectively.

He is currently with the High-Tech Institute of Xi'an. His research interests include inverse problems and its applications in neutron spectrum unfolding.

ANQI LI received the B.S. degree in information engineering from the College of Electronics Engineering, National University of Defense Technology, Hefei, China, in 2019, where she is currently pursuing the M.S. degree in information and communication engineering.

Her research interests include radio wave propagation calculation and antenna design.